nature communications



Article

https://doi.org/10.1038/s41467-025-62488-1

Utilizing alkaline solid waste for low-carbon construction material via in-situ calcium phase design

Received: 23 December 2024

Accepted: 18 July 2025

Published online: 07 August 2025

Check for updates

Bingyang He ^{1,2}, Xingyu Zhu³, Yuxin Lei⁴, Xiaohuan Jing¹, Yang Liu¹, Zhaohou Chen¹, Daqiang Cang⁵, Jean-Pierre Birat ⁶, Zian Tang ^{1,2} & Lingling Zhang ^{1,2} ⊠

Global cement market generates a large amount of greenhouse gases, driving a great interest in developing low-carbon construction materials for climate goals. Although free lime (f-CaO) and low hydration activity limit the applications in construction materials, steel slag, as an alkaline solid waste, is widely regarded as a sustainable alternative to cement. Here, we propose an in-situ calcium phase design strategy of steel slag and develop a high-performance cementitious material through pre-hydration. The pre-hydration effectively reduces the risk of the f-CaO expansion and prevents the occurrence of micro cracks. With the addition of fly ash and alkaline activator, a high elastic modulus Na-rich gel is generated and improves the material's compressive strength by 133.7%. Carbon footprint analysis indicates that the global-warming potential of the high-performance cementitious material (232–265 kg CO₂-eq ton⁻¹) is only about 34-40% of that of cement, helping to reduce about 2.2–3.0 Gt CO₂-eq from the global cement market. Interestingly, additional energy compensation (heat or microwave) is proven to expeditiously enhance the mechanical properties of the cementitious material and shorten production cycles without bringing excessive CO₂ emissions. This work inspires the strategic utilization of alkaline solid waste in a simple way.

The global consumption of cement has increased by over 30 times since 1950. More importantly, the cement industry contributed to 8% of global CO₂ emissions, becoming one of the most important contributors to climate change¹. Considering the growing demand for cementitious materials worldwide², achieving carbon neutrality in the cement industry is the outmost challenge.

The International Energy Agency (IEA) pointed out that improving energy efficiency and using cleaner fuels were key solutions for carbon reduction in a short term³. For a long term, reliable

and novel technologies are highly demanded. This encourages emerging markets and developing economies to explore more possibilities. Therefore, the exploration of potential alternatives to cement has received widespread attention. These alternatives must meet the following requirements: 1. A sufficiently low intensity of ${\rm CO}_2$ emissions; 2. A great availability for large-scale utilization; 3. Excellent physical properties (mechanical strength, durability, etc.) to meet current standards (EN197-1, GB175-2023); 4. An environmental friendly composition.

¹School of Energy and Environmental Engineering, University of Science and Technology Beijing, Beijing, China. ²State Key Laboratory of Iron and Steel Industry Environmental Protection, University of Science and Technology Beijing, Beijing, China. ³Department of Electronic and Information Engineering, Faculty of Engineering, The Hong Kong Polytechnic University, Hong Kong, SAR, China. ⁴China Environmental United Certification Center Co. Ltd., Beijing, China. ⁵School of Metallurgy and Ecological Engineering, University of Science and Technology Beijing, Beijing, China. ⁶IF Steelman, 5 Rue du Gate-Chaux, Semecourt, France. E-mail: zhangling@ustb.edu.cn

Alkali activated materials (AAMs) were considered as alternative cementitious materials with low CO_2 emissions by introducing alkaline solid waste, industrial by-products, or other aluminosilicate as precursors^{4,5}. As a bulk alkaline solid waste, steel slag (SS) powder has been introduced into AAMs. SS is of quite enormous quantity. In fact, in developing countries like China, more than 70% of SS was not effectively utilized and stockpiled randomly⁵. Based on the global crude steel production data (Fig. 1), more than 190 million tons of steel slag urgently need to be effectively utilized annually. Howerver, literature review shows that the existing technology cannot meet the great demand for the large-scale utilization of steel slag. The amount of steel slag introduced in traditional AAMs was only 10–30 wt%⁶⁻⁹.

The two main challenges hindering the strategic applications of steel slag in AAMs are the critical expansion components and low reactivity. Compared to cementitious materials mainly composed of tricalcium silicate (such as Portland cement, ground blast furnace slag), the hydration activity of steel slag with dicalcium silicate (β -C₂S) as the main crystal phase is quite unsatisfied¹⁰. Additionally, the critical expansion of free lime (f-CaO) in steel slag induced a durability risk of AAMs with the presence of water. As shown in Eq. (1), the hydration of f-CaO leads the volume expansion by 98% theoretically^{11,12}.

$$f - CaO + H_2O \rightarrow Ca(OH)_2 \tag{1}$$

To enhance the hydration activity of SS, advanced grinding techniques have been applied. The ultra-fine steel slag has received increasing attention with a specific surface area exceeding 700 m² kg⁻¹. The cementitious properties of ultra-fine steel slag have been reported in previous literature^{13–15}. Interestingly, the cementitious materials based on ultra-fine steel slag exhibited significantly high reactivity

initially, while the contribution became much less significant during the later period (after 28 days). In the long term, the amount of hydration products of ultra-fine slag did not seem to be greater than that of steel slag¹⁶. Using X-CT (X-Ray Computed Tomography), Yang et al.¹⁷ observed that the addition of ultra-fine SS adversely increased the blade-like and rod-like pore structures in cement, causing critical cracks and a decrease of compressive strength. One possible association is that during the grinding process, the inert RO phase was partially removed, while more grindable calcium phase and f-CaO exposed¹⁸. This was likely to exacerbate the volume expansion of AAMs using ultra-fine SS. Therefore, it was much more significant to remove f-CaO from ultra-fine SS.

Currently, one of the solutions is to accelerate carbonation, converting f-CaO into calcite. However, the transmission efficiency of CO_2 inside solids rapidly decreases with the increase of particle size and the accumulation of surface carbonate layers. Another issue was CO_2 enrichment to accelerate carbonation, which increased additional energy consumption. Therefore, extremely stringent conditions were required to guarantee the complete conversion of f-CaO to calcite during accelerated carbonation. As pointed out by Ravikumar et al. 19, there was a higher likelihood of negative carbon dioxide benefits when using CO_2 curing strategy for concrete. In addition, as carbonation continues, the active components (e.g., calcium silicate and portlandite) are converted into inert calcite 2O . Generally speaking, accelerated carbonation seems more suitable for well-designed prefabricated components.

Considering that the first stage of hydration involves the reaction between f-CaO and water, we speculate that the hydration process can be divided into two steps. At the beginning, the ultra-fine steel slag is mixed with excess water (referred to as pre-hydration) to remove

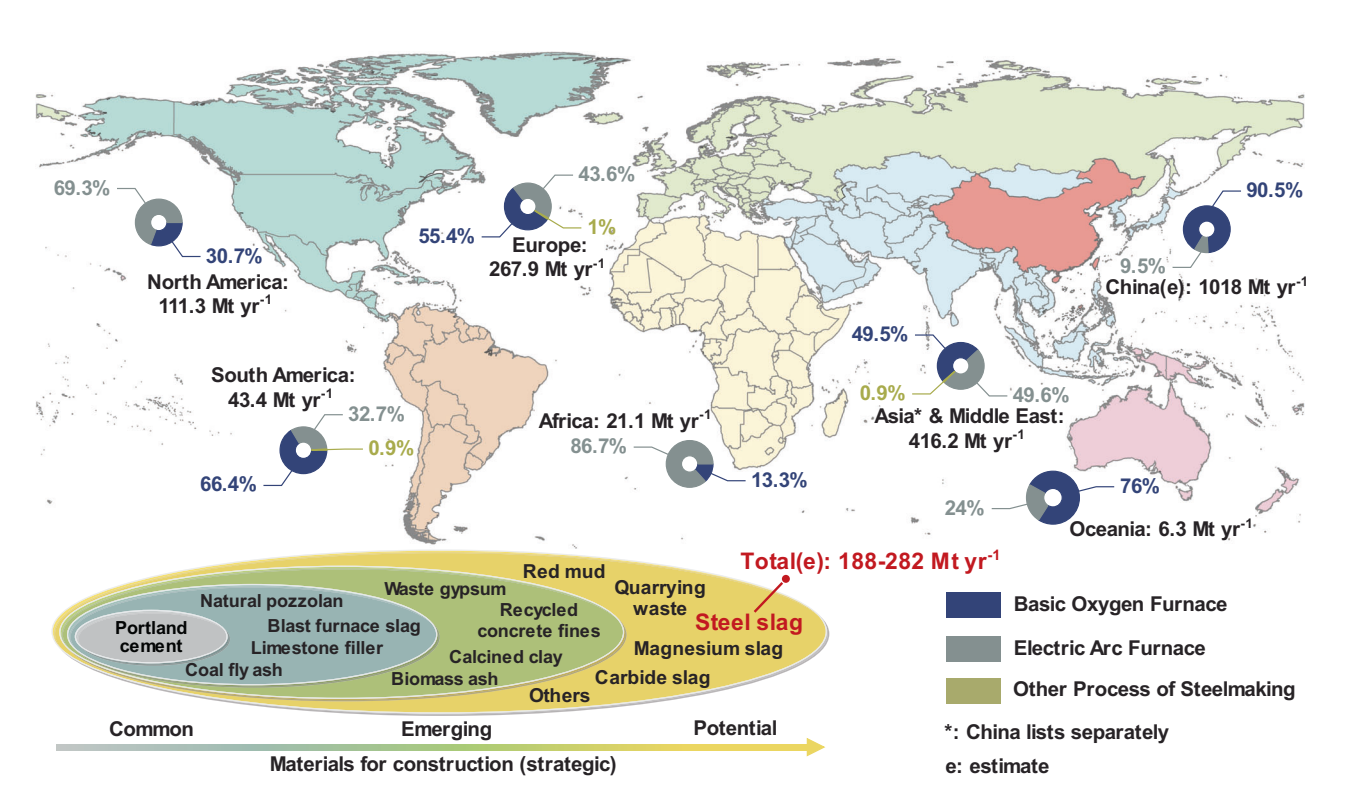


Fig. 1 | **World crude steel production and estimated steel slag generation in 2022.** China produces over half of the crude steel, followed by other regions in Asia, resulting in a large amount of stockpiled steel slag $^{42-44}$. The estimated amount of steel slag produced per ton of crude steel is 10–15%. Similar potential alkaline

solid wastes with critical expansion risks include carbide slag (40 Mt yr⁻¹)⁴⁵ and magnesium slag (8 Mt yr⁻¹)⁴⁶. The map was generated using Geographic Information Systems software ArcGIS v.10.8 (http://www.esri.com/).

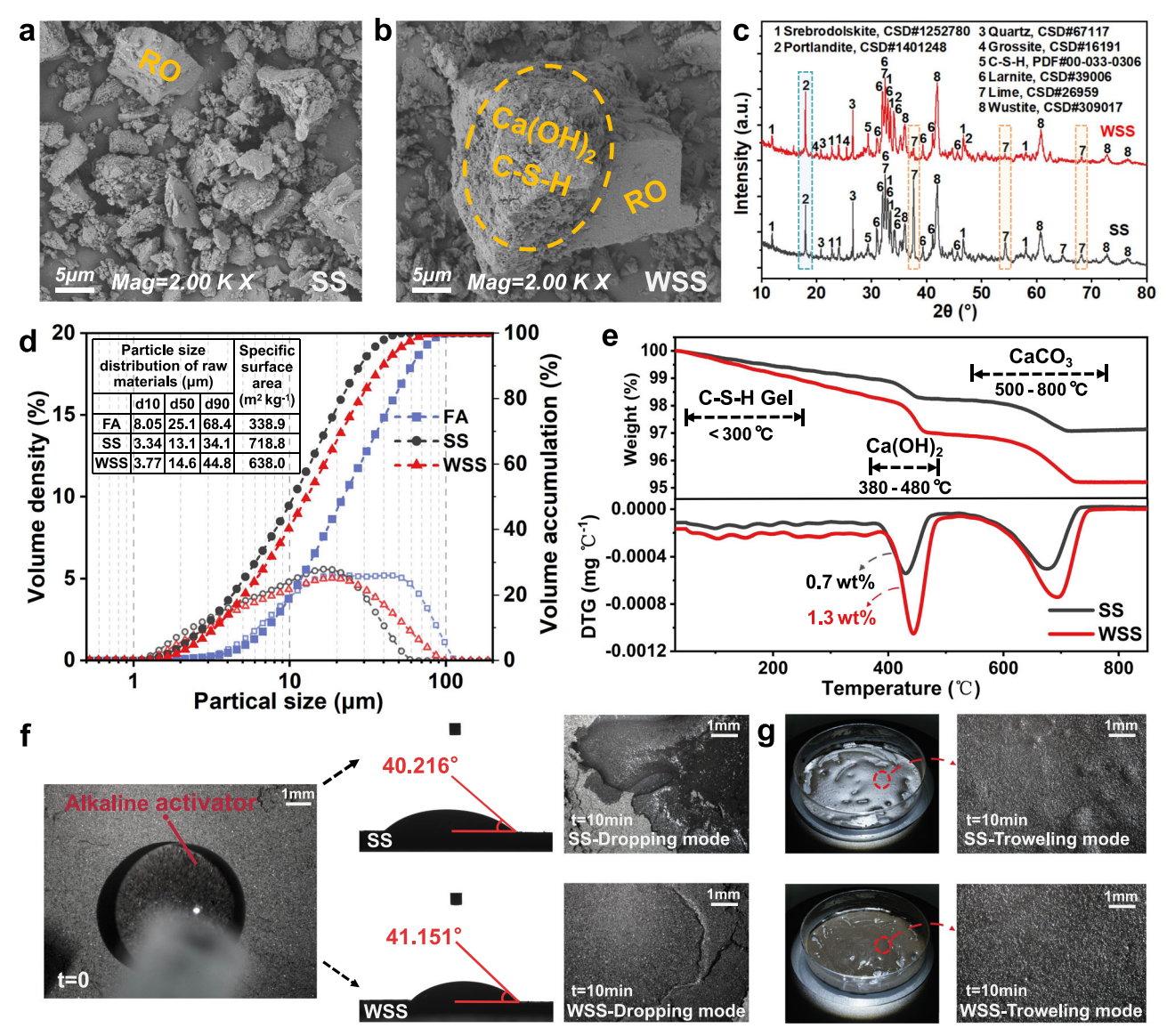


Fig. 2 | **Differences in the properties of SS (control) and WSS (experimental) powders through pre-hydration. a** The surface morphology of SS particles. **b** The surface morphology of WSS particles. **c** XRD spectra of SS and WSS. The vertical axis (a. u.) represents arbitrary units. The obvious changes after pre-hydration were the decrease of lime (blue box) and the increase of portlandite (orange box) as well as C-S-H. **d** Particle size distribution and specific surface area of three precursors (SS, WSS, and FA). Solid symbols refer to the volume accumulation value, while

hollow symbols refer to the volume density value. The dashed line indicates the trend of volume distribution of the three precursors. **e** The thermal weight loss (nitrogen atmosphere) of SS and WSS. **f** In-situ microscopic observation of the static contact angle between the precursor powders and alkaline activator, as well as the dynamic dehydration process in dropping mode. **g** Dynamic dehydration process in troweling mode.

f-CaO while avoiding excessive bonding between powders. After drying and redispersing, the ultra-fine steel slag is used as a precursor for the cementitious materials. In fact, a blind spot was easily overlooked because previous literature subconsciously associates hydration with the solidification process when applying precursor powders with high f-CaO content^{12,21,22}. As a result, the optimal modification stage was missed. Conversely, when pre-hydration is carried out before solidification, the expansion stress of f-CaO could be effectively released in advance while calcium silicate and portlandite were retained.

In this study, an in-situ calcium phase design strategy was proposed by pre-hydration. Through solid-liquid infiltration behavior adjustment, the fully industrial solid waste mixture of 70 wt% Washed Steel Slag (WSS) and 30 wt% Fly Ash (FA) was successfully used to develop AAMs, exhibiting a 133.7% increase of compressive strength compared to the SS sample without pre-hydration. Further investigation on the generation of Na-rich gel and f-CaO expansion was applied to understand the "in-situ calcium phase design" strategy. Aiming to

promote discussion on solutions to strategic application of steel slag for combating climate change, the global-warming potential of the proposed AAMs was evaluated, showing a $\rm CO_2$ emissions reduction of 2.2–3.0 Gt worldwide.

Results

Changes in pre-hydrated steel slag

After pre-hydration, the phase composition of SS changed significantly. As shown in Fig. 2a, the surface of the RO phase in the original steel slag was smooth, distinct from the other crystal phases, which was more clearly shown in Supplementary Fig. 1 with a larger field of view. In the SEM images, the RO phase showed a crystal size of over 20 μm . Small particles below 20 μm were mostly composed of calcium silicate, quartz, lime, and portlandite. These substances, mainly composed of Ca, Si, and Al, have lower hardness and are prone to forming small-sized particles during the grinding process. After prehydration, a layer of C-S-H (calcium silicate hydrate) gel and flaky

Ca(OH)₂ (Portlandite) were attached to the surface of RO phase (Fig. 2b). The increase in corresponding peaks in the XRD spectra (Fig. 2c) and the increase of weight loss in the TG curve (Fig. 2e) confirmed the generation of the above two substances. Interestingly, the average particle size D50 (Fig. 2d) increased from 13.1 µm to 14.6 µm, while D90 showed a larger increase (from 34.1 um to 44.8 um). In the differential distribution curve, an important turning point was at 20–30 µm, which supported our particle partitioning principle and the interpretation of the pre-hydration. A large amount of f-CaO with a size less than 20 μm dissolved and released Ca²⁺. During the drying process, RO phase was covered with generated Ca(OH)₂ and C-S-H, with its particle size tending towards larger values. As is well known, Ca(OH)₂ is one of the important precursors for the C-S-H, which can generate calcium silicate when silicon source was present in the environment²³. This implied that the f-CaO in steel slag had both advantages and disadvantages. The effective conversion of f-CaO to Ca(OH)2 was crucial. Additionally, the TG curve showed that carbonate products were also produced in trace amounts. This was due to the unavoidable invasion of CO₂ during the pre-hydration and drying process.

In-situ microscopic observation confirmed that pre-hydration significantly affects the infiltration behavior of alkaline activator on precursor powders. In dropping mode (Fig. 2f), The difference in static contact angle between WSS powder and alkaline activator is not significant. However, during the infiltration process of the control group, local rapid hardening of the SS powder led to an uneven diffusion of the alkaline activator. The expansion of the hardened area is attributed to the strong absorption of water by f-CaO. On the contrary, the infiltration process of the experimental group was quite smooth in Supplementary Movie 1. The alkaline activator was uniformly dispersed in the WSS powder and absorbed. In troweling mode, the alkaline activator was rapidly mixed with precursor powders in a mass ratio of 1:2. Then, The slurry was applied to the plastic dish to simulate the hardening process of the internal cross-section of the material (Fig. 2g). As time goes by, the SS slurry dried rapidly and expansion areas appeared on the surface, while the WSS slurry effectively avoided the expansion. It can be foreseen that after pre-hydration, the dispersion of precursor powders in the alkaline activator has been improved, obtaining a uniformly hardened cementitious material.

Considering the environmental impact caused by inevitable leaching during reuse, special attention was paid to the heavy metal element Cr and inorganic elements P and S in the wastewater, as the mass fractions of their oxides in the original steel slag reached 0.236 wt%, 2.047 wt%, and 0.225 wt%, respectively (Supplementary Table 1). The leaching results (Supplementary Fig. 2) showed that the total Cr and total P concentrations were only 0.011 mg L $^{-1}$ and 0.024 mg L $^{-1}$, respectively, which were far below the industrial wastewater limit standards (0.05 mg L $^{-1}$ and 0.1 mg L $^{-1}$, GB 3838-2002). This may be because the alkaline condition limits the leaching of Cr and P. The concentration of S reached 22.491 mg L $^{-1}$, and when converted to SO4 $^{2-}$, it is 67.473 mg L $^{-1}$. Although still below the standard (250 mg L $^{-1}$), it could not be denied that the S was more easily leached than Cr and P in steel slag.

Improved performance of AAMs due to pre-hydration

The typical heat evolution curve of Portland cement shows three distinct stages, namely the induction period (before 3 h), the main hydration period (3–24 h), and the post-hydration period (after 24 h)²⁴. The generation of needle-like C-S-H during solidification led to the appearance of the hydration peak. However, in the hydration process of steel slag-based AAMs, the addition of alkali activator greatly boosted the heat evolution. As observed in Fig. 3a, the reaction released a large amount of heat in the first 8 hours, and then gradually became smooth and remained at a low heat release. There was no hydration peak during the entire curing process. This was consistent with the research results of Liu et al.⁶ The precursor rapidly dissolved

and reacted in an alkaline environment, forming a dissolution peak (Supplementary Fig. 3) in about 6 minutes. After pre-hydration, the peak value of the dissolution heat decreased from 50.9 mW g⁻¹ to 46.0 mW g⁻¹. In the first 6 hours, the heat release of the pre-hydration group decreased by 16.71/g, and the cumulative heat release decreased by up to 26.2% (about 27 J g⁻¹) after 3 days. Furthermore, according to the TG curve (Fig. 2e) and thermodynamics, the pre-hydration of f-CaO in the WSS sample avoided approximately 15.2 \lg^{-1} of heat release (Supplementary Methods 1), accounting for over 90% of the difference in heat release between SS and WSS samples in the first 6 hours. This result strongly supported the significant influence of f-CaO on cementitious materials. Less heat release reduced the evaporation of water. On the one hand, it was beneficial for delaying the solidification of the slurry. Figure 3h demonstrated that the dynamic viscosity of WSS slurry consistently remained at a lower value. On the other hand, rapid water loss around f-CaO did lead to local dehydration, which in turn affected the pore structure (Fig. 3b and 3i) as well as the hydration and pozzolanic reaction.

Interestingly, the experimental group showed a platform stage at 2-6 h (Fig. 3a), indicating that the samples had an unconventional exothermic behavior. Some studies have pointed out that this stage was consistent with the dissolution of [SiO₄] from the fly ash^{6,25}, which may suggest a rapid pozzolanic reaction. In Fig. 3c, d and Supplementary Fig. 4, the experimental group showed a more significant weight loss between 50-300 °C, indicating a higher content of hydration products. The left shift of Si-O bending vibration band (about 450 cm⁻¹)²⁶ in the FITR spectrum (Fig. 3e, f) also confirmed that more gel was generated. In most studies, the introduction of FA mainly played two roles. From the physical perspective, finer FA beads could act as a pore filler, and their smooth surface increased the fluidity and processability of the AAMs slurry. From the chemical perspective, the [SiO₄] and [AlO₄] from FA were attacked and depolymerized by OH in an alkaline environment²⁷, becoming the precursor of Na-rich gels which was similar to the hydration products of Portland cement.

In addition, the compressive strength of AAMs under three curing processes (RT, room temperature. MW, microwave. OV, oven heating) at 7 d and 28 d was statistically analyzed, representing the early and longterm mechanical performance (Fig. 3g). The control group samples did not reach the equivalent strength standard of P.O 42.5R at 28 d, regardless of the introduction of additional energy. However, the prehydration group sample achieved a compressive strength of 55.6 MPa at 28 d at room temperature, far exceeding P.O 42.5 R. This demonstrates the positive contribution of pre-hydration to the mechanical performance development of the samples and suggested that it could reach sufficient performance without the input of additional energy. The compressive strength of WSS OV sample at 7 d had exceeded 50 Mpa. Furthermore, Supplementary Fig. 5 demonstrates the reliability of using alkaline wastewater (Wa) to prepare alkaline activators. However, with accelerated hydration reactions and the formation of gel phases, even under 70 °C, the late-stage activity of WSS OV was consumed prematurely. The slight change in the weight loss curve at 50-300 °C confirmed that its late-stage reaction was limited. Rapid consumption of water in the early stage led to a reduction in the available water for later use, which was detrimental to the strength development of AAMs in the long term. And this phenomenon was particularly evident in the control group with more pores and cracks. On the contrary, AAMs at room temperature curing and microwave curing maintained good strength development in the later stages. In particular, microwave-cured AAMs seemed to exhibit a most complete hydration. Both the control group and the experimental group achieved the highest mechanical performance within their groups. It was important to note that there were two distinct approaches when designing microwave curing experiments: short-term & high-power mode, and long-term & low-power mode²⁸. Preliminary experiments have shown that the long-term & low-power

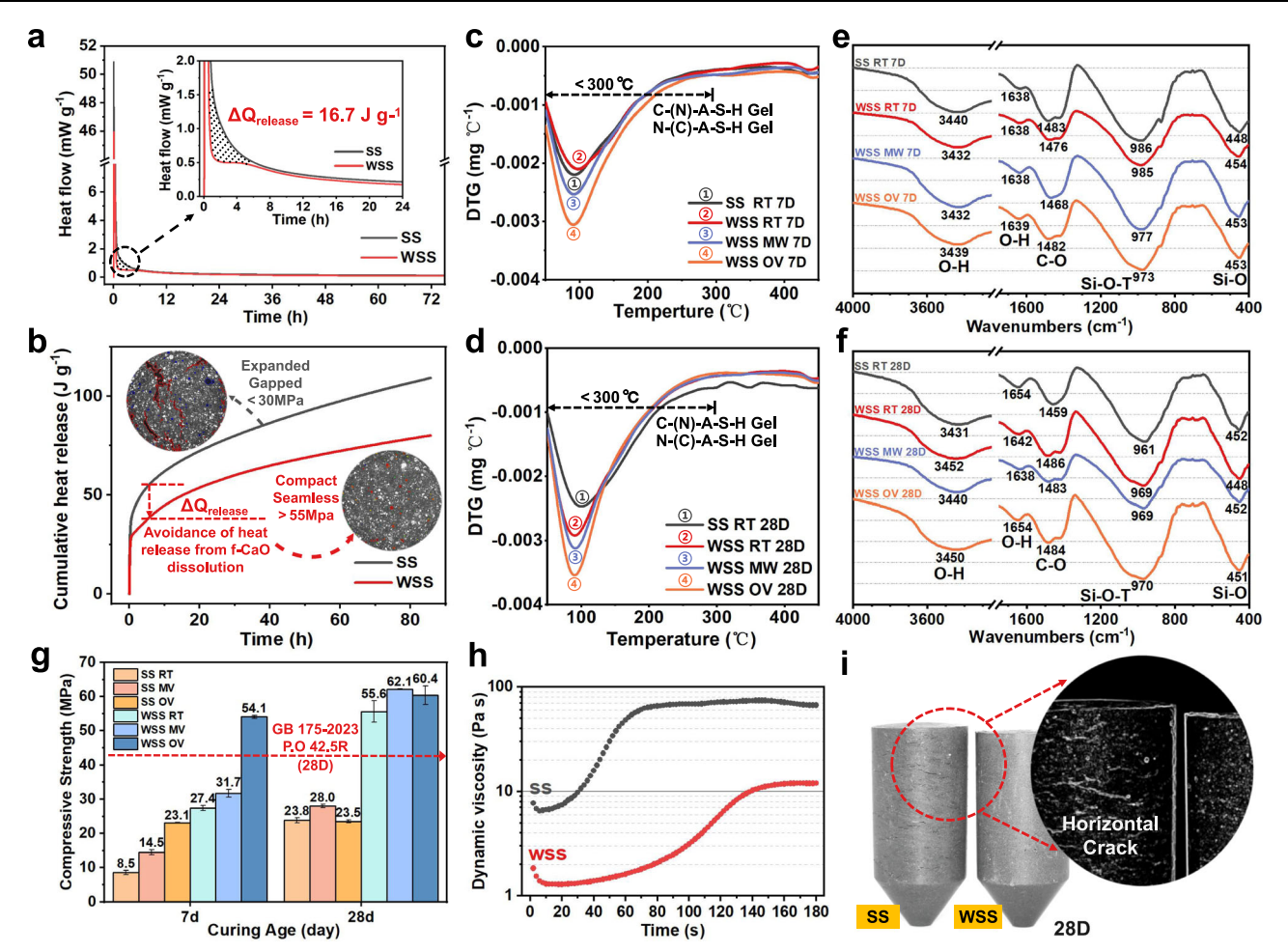


Fig. 3 | **Effect of pre-hydration strategy on the performance of steel slagbased AAMs.** a Differences in heat flow of AAMs due to pre-hydration strategy. The inset figure shows the difference in heat flow between two groups of samples in the first 24 hours. **b** Differences in cumulative heat release of AAMs due to pre-hydration strategy. **c** Thermal weight loss of AAMs (7 d) under different processes (RT, room temperature. MW, microwave. OV, oven heating). In the image, the C-(N)-A-S-H gel and N-(C)-A-S-H gel are respectively hydrated calcium silicate gel and hydrated sodium silicate gel. The main difference between the two substances lies

in the content of Na $^+$ and Ca $^{2+}$. **d** Thermal weight loss of AAMs (28 d) under different processes. **e** FTIR spectra of AAMs (7 d) under different processes. **f** FTIR spectra of AAMs (28 d) under different processes. **g** Compressive strength development of AAMs under different processes. The error bar represents the standard deviation of the test samples and the mean represents the strength value (n = 3). **h** Dynamic viscosity curves of SS slurry and WSS slurry. **i** Images of the experimental group and control group samples. The details in the zoomed in image show the orientation and distribution of surface cracks on the two samples.

mode could also lead to severe water loss and even sample cracking due to the strong absorption of microwave by polar molecules such as H_2O .

Microstructural differences in AAMs due to pre-hydration

In the early stage (7 d), the control group samples showed a large number of cracks and pores, some of which were nearly 100 μ m in diameter (Fig. 4a). We investigated the chemical substances around the large pores and could clearly see flaky Ca(OH)₂ grains (Fig. 4b and Supplementary Fig. 6b), most of which were 2-3 μ m in size. It could be seen that in a water-deficient environment, a large amount of Ca(OH)₂ could not continue to participate in the hydration reaction or pozzolanic reaction. At 28 d, the honeycomb-like C-(N)-A-S-H gel could be observed²⁹. However, large particles of FA have not been dissolved (Fig. 4c), and gaps were observed between FA particles and the substrate, proving that the pozzolanic reaction was insufficient in this condition. The EDS results (Supplementary Fig. 6a) showed the chemical composition of the C-(N)-A-S-H gel was with a Ca/Si ratio of about 0.9. A small amount of Na⁺ was introduced to the gel, with a Na/Ca ratio of about 0.7.

In comparison, the experimental group samples had fewer pores and cracks. In Fig. 4d, e, unlike the control group, flaky N-(C)-A-S-H nano crystals were observed. The crystals were stacked layer by layer

until the overall structure loses its distinct crystalline structure. This kind of Na-rich gel was rarely been mentioned in previous studies. It was generally believed that alkali-activated products were colloidal substances similar to cement hydration. However, here we did observe the different forms of N-(C)-A-S-H gel at 7 d, which had similar chemical compositions. EDS results showed that the Na/Ca ratio of N-(C)-A-S-H gel reached an astonishing 2-2.5 value (Supplementary Fig. 6c). In Fig. 4f, FA particles with a shell wrapped in sodium hydroxide crystals were observed, indicating that pozzolanic reaction was still ongoing. Supplementary Fig. 7 and Supplementary Fig. 8 provide a clearer record of the growth of NaOH crystals on the surface of FA particles. More interestingly, AFM results showed that the N-(C)-A-S-H gel had higher elastic modulus, reaching about 30 GPa in the early stage (Fig. 4g, h). And the elastic modulus strength of N-(C)-A-S-H gel increased to an astonishing 50 GPa at 28 d, which was much higher than that of C-(N)-A-S-H gel. This value was also higher than the hydration product of common cement (C-S-H gel, 30–40 Gpa^{30,31}). The mechanical properties of interface transition zone between unreacted FA particles and C-(N)-A-S-H gel or N-(C)-A-S-H gel was shown in Supplementary Fig. 9. This proved that pre-hydration not only improved the pore structure of AAMs, but also improved the mechanical strength and adhesive properties of gel through Na⁺ enrichment.

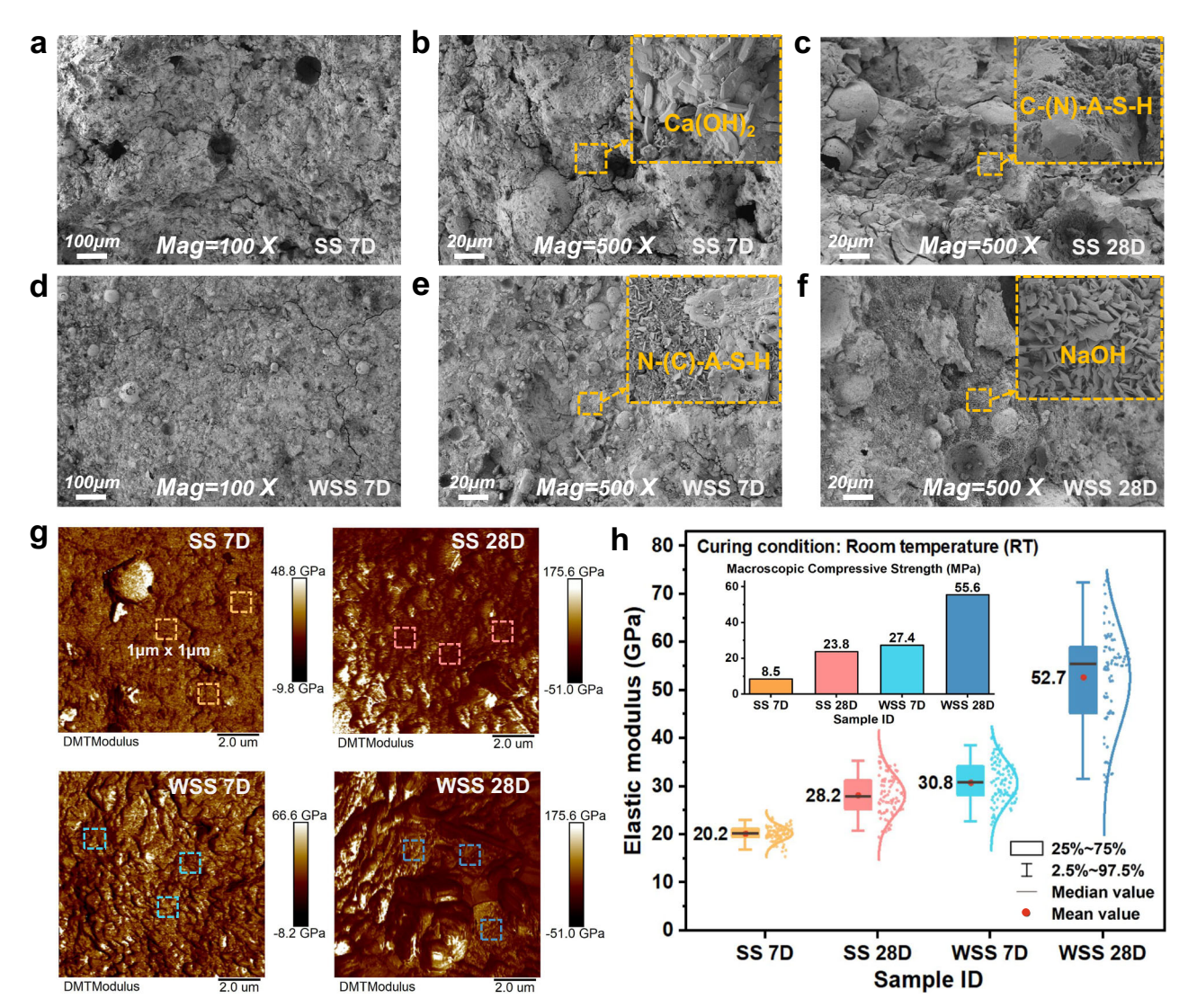


Fig. 4 | **SEM** and **AFM** images of the control and experimental group samples. **a** Microstructure of AAMs prepared at 7 d using SS, magnified 100x. **b** Microstructure of AAMs prepared at 7 d using SS, magnified 500x. A large number of calcium hydroxide crystals were observed. **c** Microstructure of AAMs prepared at 28 d using SS. Compared to 7 d, The pore structure was improved, and the main gel phase was C-(N)-A-S-H. Unreacted fly ash was observed. **d** Microstructure of AAMs prepared at 7 d using WSS, magnified 100x.

e Microstructure of AAMs prepared at 7 d using WSS, magnified 500x. Fewer cracks

and pores were observed, and the main gel phase was N-(C)-A-S-H. **f** Microstructure of AAMs prepared at 28 d using WSS. Sodium hydroxide crystals were observed to be distributed around the fly ash. **g** Elastic modulus distribution of different gels. **h** The elastic modulus of the gel in the four samples in Fig. 4g was extracted and plotted in box plots, with data (n = 81) obtained from orange, red, light blue, and dark blue boxes in Fig. 4g, respectively. Confidence interval 95%. The median value represents the average elastic modulus of the sample. The inset figure shows the macroscopic compressive strength corresponding to four samples.

In order to obtain an accurate 3D structural characteristic of micron-scale pores and cracks, X-CT was applied. After segmentation of pores using a grayscale threshold, the two groups of samples showed completely different pore structure characteristics. The control group samples showed an astonishing porosity (Fig. 5g). In Fig. 5b, the widest part of the crack exceeded 30 µm. The ribbon-like distribution characteristics in Fig. 5c confirmed the previous conjecture that the growth of cracks always extended along a certain plane. Combined with transparent test tube experiments (Supplementary Movie 2), we speculated that during the initial curing process, the expansion of f-CaO caused local stress concentration. Since the upper part of the mold was unconstrained, a vertical tearing force was generated, which ultimately led to transverse cracks (Fig. 5h). Interestingly, as shown in Fig. 5a, b, FA were always presented at one end of the cracks, with an average particle size ranging from 30-80 µm. Since grayscale in CT images represents the density of matter (essentially responding to the transmittance of x-rays), it could be determined that these light gray FA particles were in an unreacted state, which was also confirmed by SEM images (Fig. 4c). During the development of pores, these unreacted FA likely promoted the extension of cracks due to local stress concentration instead of contributing to the pozzolanic reaction. Although there were also large particles of FA that had not been completely dissolved, the CT images of the experimental group (Fig. 5d-f) clearly showed a tight connection with the substrate. Therefore, almost no cracks were observed in the experimental group of samples, which was consistent with the SEM results. Like the Butterfly Effect, the presence of f-CaO not only deprived a large amount of water, but also led to irreversible expansion and heat release, further exacerbating water loss. X-CT images also suggested that some large sized FA particles hardly reacted with the alkaline activator, ultimately accelerating crack generation.

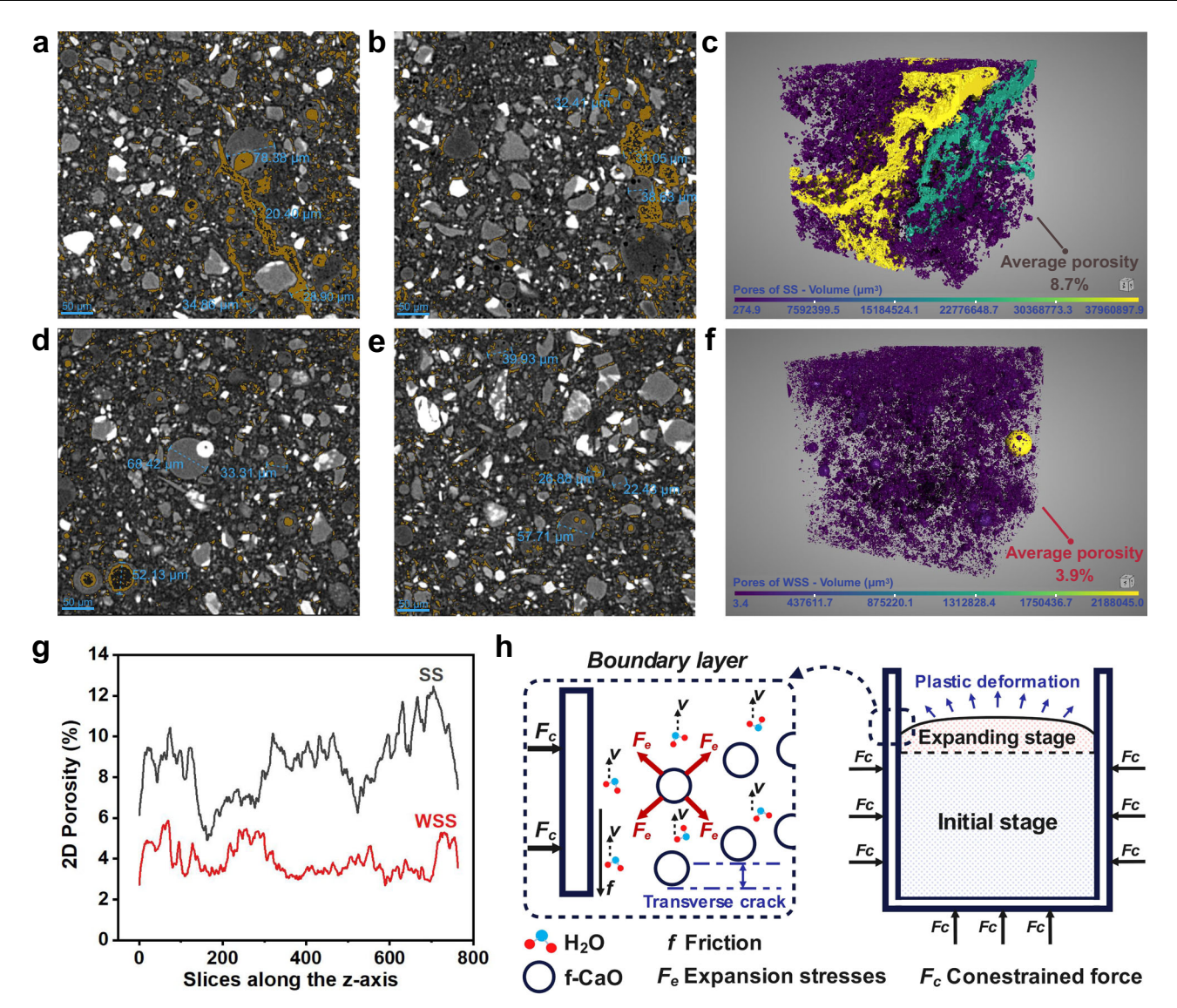


Fig. 5 | X-CT images of the control and experimental samples. a 2D slice of the control group sample, cracks were marked with yellow highlights. b Another 2D slice of the control group sample. c Pores and cracks in the control samples were identified and extracted, with an estimated average porosity of 8.7% (resolution: 1.5 μ m). d 2D slice of the experimental group sample. e Another 2D slice of the experimental group sample. f Pores and cracks in the experimental samples were identified and extracted, with an estimated average porosity of 3.9% (resolution:

 $1.5~\mu m).~g~2D$ porosity of control and experimental group samples based on X-CT. Slice thickness: $1.5~\mu m$. Number of slices: 763.~h Due to the expansion of f-CaO occurring during the material hardening process, the control group sample undergoes plastic deformation. Along the unconstrained direction (upward), the concentration of expansion stress leads to transverse cracks. Considering the friction on the mold wall, the actual expansion shape of the control group sample shows a convex shape.

Carbon footprint analysis of steel slag-based AAMs

In China, it is common for steel companies to sell ground blast furnace slag (for cement admixture, 150-200 ¥ ton¹) to cement companies. Here, steel slag-based AAMs are suggested to be sold directly as low-carbon cementitious materials (for cement replacing, 350–400 ¥ ton¹). Manufacturing steel slag-based AAMs is considered profitable for both steel and cement companies. But for steel companies, producing steel slag-based AAMs on their own obviously had lower costs and higher production efficiency. Therefore, we assume that steel slagbased AAMs are produced and sold by steel companies. Due to the unavoidable generation of solid waste such as SS and FA, it is considered an industrial byproduct and does not generate excess GHG emissions. Under the same boundary division in Supplementary Fig. 10, the GHG emissions of steel slag-based AAMs was estimated and compared with materials such as general cement and LC³ cement (Limestone Calcined Clay Cement).

Carbon footprint analysis showed that the carbon emissions from the production of steel slag-based AAMs were much lower than those from general cement and LC3 cement (Fig. 6a). This is mainly attributed to the complete avoidance of the large amount of CO₂ generated by limestone calcination. Although LC³ is also considered a promising lowcarbon cementitious material, it is difficult to completely avoid using common cement. Maintaining a replacement rate of 15-50% is necessary to ensure reaching the strength standard of P.O 42.5 R cement³²⁻³⁴. During the manufacturing process of AAMs (RT), the GHG emissions from the production of alkaline activator accounted for 64.7% (150 kg CO₂-eq ton⁻¹), exceeding the sum of grinding, drying, transportation, mixing, and other steps. Even under oven curing and microwave curing conditions, the CO₂ emissions from the production of alkaline activator still exceeded 58% (Fig. 6c-e). In possible cases, reducing the use of alkali activators would significantly reduce the carbon emissions of steel slag-based AAMs. The NaOH crystals observed in the WSS samples in our

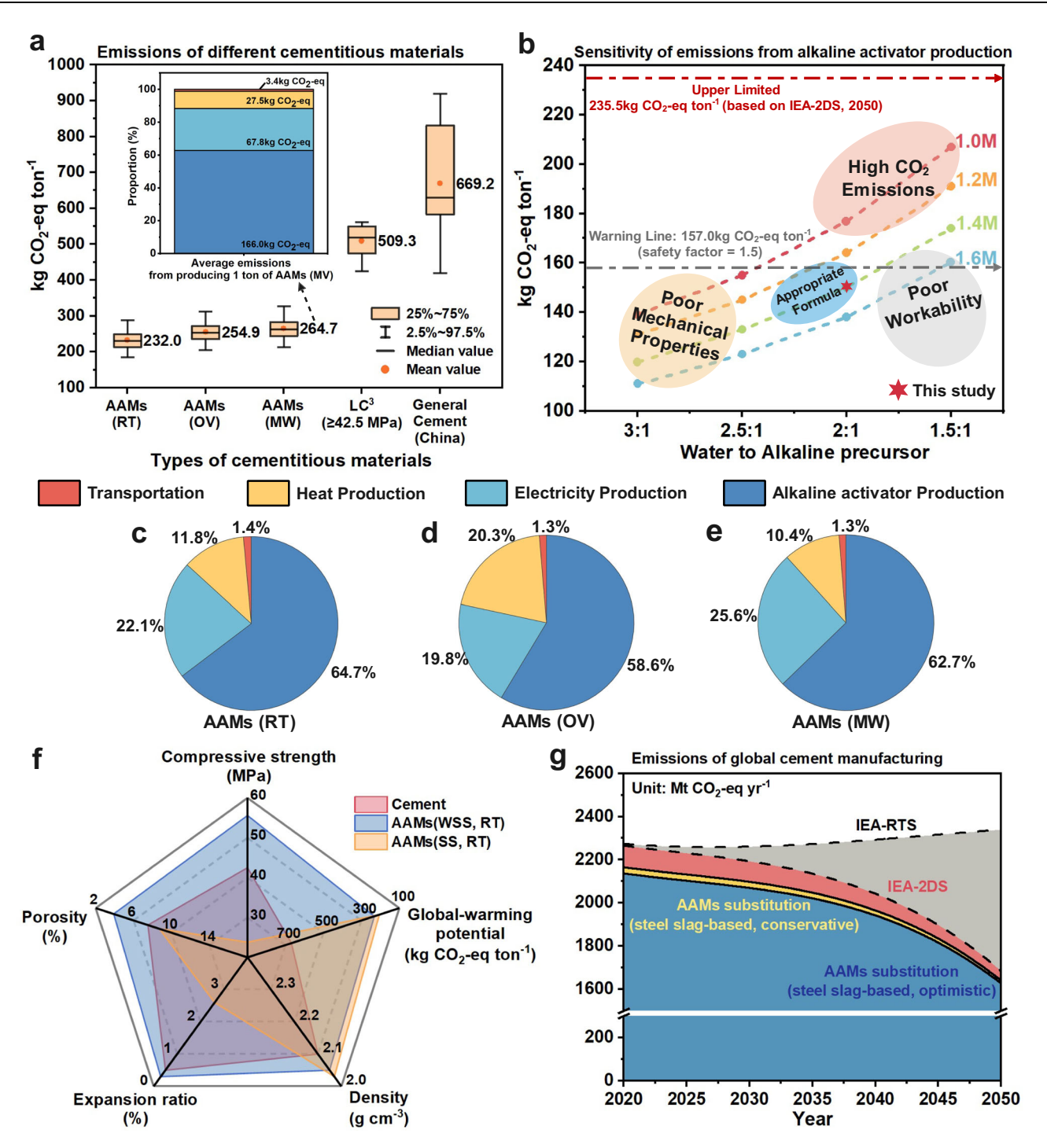


Fig. 6 | **Carbon Footprint Assessment of steel slag-based AAMs. a** Estimation of GHG emissions per unit mass of steel slag-based AAMs produced under different curing processes. The source data for the box plot is obtained through Monte Carlo uncertainty analysis, with 5000 simulated runs for each process. Confidence interval 95%. The median value represents the average GHG emissions of the process. In the inset figure, the energy consumption and proportion of each department of AAMs MW are displayed (calculated by mean value). **b** Sensitivity analysis of alkaline activator production to GHG emissions. The dashed line indicates the trend of GHG emissions from alkaline activator production with varying concentrations of the alkaline precursor at a specific modulus of sodium silicate (1.0

M–1.6 M). c Percentage of GHG emissions by stage for AAMs (RT). d Percentage of GHG emissions by stage for AAMs (OV). e Percentage of GHG emissions by stage for AAMs (MW). f Comparison of main properties between steel slag-based AAMs and cement. Specifically, the density of the cementitious material is considered to be as low as possible. g The impact of using steel slag-based AAMs as a substitute on GHG emissions from global cement manufacturing. RTS, Reference Technology Scenario. 2DS, 2 Degree Celsius Scenario. The conservative scenario assumes a steel slag generation rate of 10% during the crude steel manufacturing process, while the optimistic scenario assumes a rate of 15%.

experiments indicated that the AAMs were likely still water-deficient or excessive amounts of alkaline precursors had been added.

Figure 6b showed the impact of sodium silicate modulus (molar ratio of SiO₂/Na₂O) and concentration (water:alkaline precursor) on

GHG emissions. Based on a standard of 364 kg CO₂-eq ton⁻¹ (IEA's projected global average cement GHG emissions in 2050³⁵), the upper limit of GHG emissions generated by the alkaline activator has been determined to be 235.5 kg CO₂-eq ton⁻¹. Considering the lack of

wastewater filtration, labor, management, or longer transportation distances for materials, a safety factor of 1.5 wass used to determine a GHG emission warning line of 157 kg $\rm CO_2$ -eq ton⁻¹. When the modulus of sodium silicate was set between 1–1.2 M, a high proportion of NaOH addition was required and led to a high GHG emissions. Relatively, when the modulus of sodium silicate exceeded 1.6 M and the water content was insufficient, AAMs hardened quickly and faced the risk of poor workability. According to this study, a water-to-alkali precursor ratio slightly higher than 2:1 was more suitable. This formula achieved a good balance between mechanical properties, workability, and GHG emissions. In fact, a group of experimental samples with an additional 8 g of water added were also prepared and achieved better workability and higher mechanical properties at 28 d.

Interestingly, in this study, there was no significant difference in GHG emissions between oven curing and microwave curing, and even in most runs (Supplementary Fig. 11), microwave curing required more energy consumption and emitted more CO₂. And it was inconsistent with the previous literature^{36,37} that stated that microwave heating had lower carbon emission benefits. On the one hand, this was due to the fact that the oven curing time in this case was set at 6 hours, rather than the 24 hours used in most literature. More critically, in most laboratory carbon emission calculation cases, researchers were accustomed to use the monitored power consumption of the oven as the input value. However, when considering the higher thermal efficiency of industrial heating furnaces compared to laboratory equipment, the previous laboratory calculation method might overestimate the energy consumption of oven curing. Therefore, based on the energy conversion calculation strategy, an indirect method to estimate the power consumption of industrial heating furnaces was developed. The core is that the theoretical heat absorption of AAMs remains constant across different devices, and systematic errors in laboratory calculations can be effectively avoided. On the other hand, when evaluating the energy density of microwave processes, we believe that the efficiency of microwaves has been overestimated. In this study, the energy density of microwave was approximately 100 W kg⁻¹ AAMs. with a heating duration of 16 minutes, which meant that the microwave power consumption for curing 1 ton of AAMs was 39.3-47.7 kW h (assuming an energy conversion efficiency of 56-68% for industrial microwave equipment). Compared to the oven curing, the proportion of GHG emissions caused by electricity production has increased from 19.8% to 25.6%. In previous studies, considering the different weights of materials, researchers might have used higher microwave power densities (Supplementary Table 8).

Overall, when applying pre-hydration strategy, steel slag-based AAMs outperformed cement in terms of mechanical properties, pore structures, and global-warming potential (Fig. 6f). Compared to conventional cementitious materials, lower porosity could indicate better durability and corrosion resistance. In the cement-roadmap of IEA 2DS, considering that steel slag has not yet been listed as a satisfied alternative precursor^{35,38}, effectively applying steel slag-based AAMs will remove an extra 2.2–3.0 Gt of GHG emissions (Fig. 6g and Supplementary Fig. 12).

Discussion

Pre-hydration effectively converted f-CaO in steel slag into $\text{Ca}(\text{OH})_2$, and the CO_2 emissions of the entire process were satisfactory. Alkaline wastewater could be reused to prepare alkaline activator. The harm of f-CaO to steel slag-based AAMs was multifaceted. Intense heat release led to local dehydration and particle aggregation, while the expansion of $\text{Ca}(\text{OH})_2$ crystals intensified stress concentration. As a result, the hydration products were significantly reduced, and the cracks would be difficult to self-heal. More importantly, in this case, Na^+ was hardly introduced to the hydration gels, and it was difficult for large particles of fly ash to dissolve, which promoted the growth of cracks.

In China, more than 100 million tons of steel slag and more than 150 million tons of fly ash are generated every year. Our research indicates that the pre-hydration strategy allows for the extensive use of steel slag to prepare low-carbon cementitious materials. Here, room temperature cured AAMs already reached sufficient strength, which meant that precursors could be transported in powder form and operated on-site (Fig. 7). Oven curing and microwave curing required the AAMs to be prefabricated components, and then transported to the site for assembly. Oven curing was suitable for scenarios that required rapid construction and high early strength. However, the thermal conductivity efficiency was extremely sensitive to the size of the material, which limited the practical application of oven curing. Microwave curing, on the other hand, was almost unaffected by the size of the material, and the radiation region could be flexibly adjusted according to the needs. Although the energy consumption was slightly higher, microwave curing showed more application potential in the future compared to oven curing. In addition, microwave curing could also be applied to 3D concrete printing, which is an emerging technology.

Overall, in order to achieve carbon neutral in the construction industry and sustainable development in the metallurgical industry, this study provided some insights into the large-scale utilization of steel slag. Our study showed that steel slag-based AAMs with prehydration strategy satisfied most application scenarios in terms of mechanical properties and $\rm CO_2$ emissions. Billions of tons of steel slag and fly ash have the opportunity to be effectively utilized, while bringing 2.2–3.0 Gt of carbon reduction.

Methods

Chemicals and raw materials

The ultra-fine steel slag (SS) powder was provided by a steel company in Jiangsu, China. The fly ash (FA) was supplied from Hinggan League, Inner Mongolia Autonomous Region, China. Supplementary Fig. 13 shows the crystal phase composition of FA. The industrial grade sodium silicate modulus was 2.05 M (molar ratio of SiO₂/Na₂O), and the sodium hydroxide (analytical pure, 99%) was purchased from Aladdin Reagent (Shanghai) Co., Ltd. X-ray fluorescence spectroscopy (Shimadzu XRF-1800, Japan) was used to quantitatively determine the elemental (oxide) content of the precursor powders (Supplementary Table 1). The Fundamental Parameters (FP) method was used to correct for matrix effects. The particle size distribution and specific surface area of the precursor powders were examined using a micrometer laser particle sizer (Mastersizer 2000).

Pre-hydration for steel slag

As shown in Supplementary Fig. 14, steel slag was mixed with deionized water at a mass ratio of 1:2 in a tray. Stirring for 2 minutes to fully mix. After standing for 3 minutes, preliminary solid-liquid separation was carried out, and the solids (actually in slurry state) were dried for 12 hours at $105\,^{\circ}$ C, then ground to less than $105\,\mu$ m as washed steel slag (WSS). On the other side, the liquid was left to stand for 12 hours and then filtered. The supernatant (alkaline wastewater) was used to prepare the alkaline activator. The filtered residue was also collected and used as WSS. During the pre-hydration process, the yield of WSS powder slightly exceeds 100% due to an increase in bound water, while the recovery rate of wastewater is approximately 90%.

Preparation of AAMs

Firstly, the alkaline activator used in this study has a modulus (molar ratio of SiO_2/Na_2O) of 1.4 M, which was a mixture of sodium silicate and sodium hydroxide. Deionized water or alkaline wastewater was used separately to prepare the alkali activator according to a mass ratio of 2:1 (liquid:alkaline precursor). Then, the alkali activator was stored for 24 hours before use to release heat and cool down to ambient temperature.

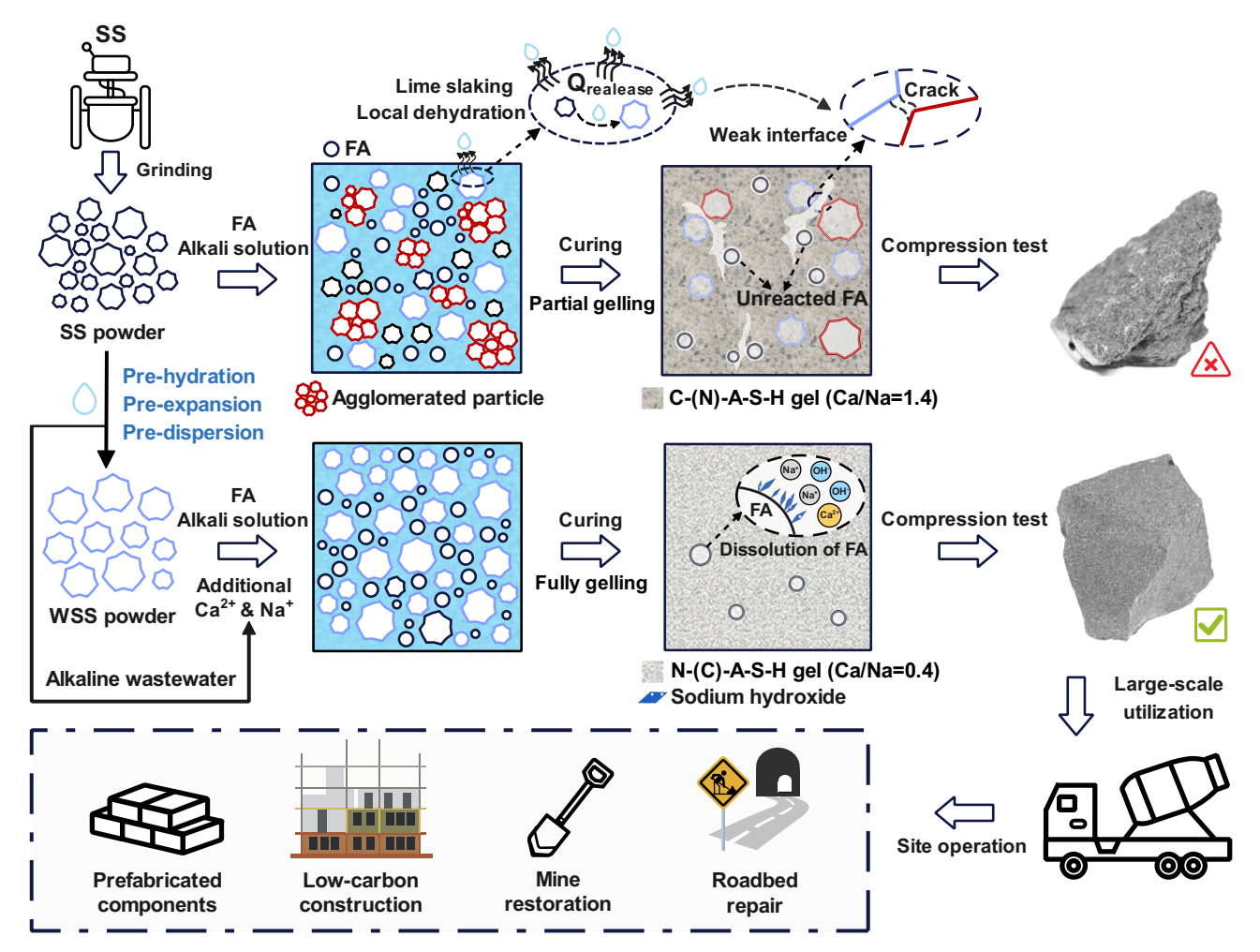


Fig. 7 | **Strategic utilization of steel slag by pre-hydration strategy.** WSS powder was introduced into AAMs at a mass fraction of 70%, while FA powder was introduced at a mass fraction of 30%. According to the application scenario, steel slag-based AAMs can be pre-processed into prefabricated components or operated on-site.

The SS/WSS and FA powders were passed through a 105 μ m sieve and well mixed according to a mass ratio of 7:3. The alkali activator and solids were stirred at a liquid-solid ratio of 1:2 for 2 minutes to prepare the AAMs paste, which was then placed on a vibrating machine for 2 minutes to remove air bubbles, and cast into a square stainless steel mold with an internal size of 40 mm \times 40 mm, wrapped in plastic film to prevent moisture loss. Therefore, for manufacturing a set of AAMs samples (n = 3), 50 g of alkaline activator, 90 g of FA, and 210 g of SS or WSS are added. Among them, the alkaline activator contains 33.33 g of deionized water or alkaline wastewater, 14.46 g of sodium silicate, and 2.31 g of sodium hydroxide.

After being placed at room temperature ($20\pm1^{\circ}C$) for 24 hours, the mold was released. Subsequently, the AAMs were placed in different environments for curing. Room temperature (RT) curing: $20\pm1^{\circ}C$; Oven (OV) curing: $70^{\circ}C$, 6 hours;,Microwave (MW) curing: $70^{\circ}W$, 16 minutes. To avoid possible uneven heating, for microwave curing, 6 blocks of AAMs (about 716 g) were symmetrically placed on a rotating tray and heated. And inspired by Kong et al.³⁹, the microwave was performed twice, that is, microwave for 8 minutes firstly, then rest for 10 minutes to prevent excessive moisture loss due to excessive temperature, and then microwave for another 8 minutes. After the curing process, the sample was placed at room temperature and aged for the test days (7 d, 28 d). To sum up, the designed mixture details are listed in the Supplementary Table 2.

Before the 7 d and 28 d, in order to prevent the hydration of the AAMs inside, the solvent exchange method was used to remove the

free water in the hardened AAMs. First, an isopropanol solution was prepared as an organic solvent. Then, the samples were placed in the isopropanol solution for 48 hours to ensure that the free water was fully removed. Then, the samples were stored on a vacuum drying oven for 24 hours at 40 $^{\circ}$ C, and finally tested.

Performance testing and microstructure characterizations

According to GB/T 17671-2021, a universal compression testing machine with a loading rate of 2.4 kN s⁻¹ was used to carry out the compressive strength tests of AAMs. The average value of the measurements of 3 samples (n = 3) taken from each group was recorded as the actual value.

X-ray diffraction (XRD, Bruker D8 advance, Germany) was used to determine the phase composition of precursor powders and AAMs, using Cu target radiation with a wavelength of 1.5416 angstroms; the working conditions were at 40 kV and 40 mA (10–80°, step width of 0.02°, scan rate of 2° min $^{-1}$).

A microscope and surface tension analyzer (Dataphysics OCA20, Germany) are used to observe the contact and infiltration behavior between precursor powders and alkaline activator. The static contact angle results were measured using the average of 3 tests. In addition, the microscopic observation results were recorded by the camera with a 3-second interval between each photograph, and presented as Supplementary Movie 1. And in order to observe the spatial orientation of the AAMs cracks, samples were cured in transparent test tubes. The expansion and hardening process of SS/WSS slurry was recorded with a 5-second interval (Supplementary Movie 2).

Isothermal conduction calorimetry (TAM Air 8-channel microcalorimeter, USA) was used to record the early thermal evolution of AAMs at room temperature to compare the differences in exothermicity caused by using different precursors. 10 g of precursor powders and 5 g of alkaline activator were stirred for 1 minute using an internal stirrer and left at room temperature until the 3 d age. The heat data during this period was automatically recorded by the calorimeter.

The dynamic viscosity of SS slurry and WSS slurry was measured using an MCR 502e rheometer (Anton Paar, Austria) at 25 °C. 20 g of alkaline activator and 40 g of precursor powders were quickly mixed and poured into the mold, and the dynamic viscosity curve of the slurry for the first 3 minutes was recorded. The shear rate was set to $10 \, \text{s}^{-1}$.

Scanning electron microscopy (SEM, ZEISS Sigma 300, Germany) was used for the microstructure observation of precursors and AAMs. Prior to imaging, samples were dried in a vacuum and coated with a thin layer of gold. The samples were observed at a magnification of 100–40,000 times under an accelerating voltage of 3 kV. And the chemical compositions of specific products in different samples were determined using an energy spectrometer (EDS).

The mass loss of the precursors powders as well as the AAMs samples (ground to 74 $\mu m)$ under a nitrogen atmosphere was analyzed by thermogravimetry analysis (TG, Mettler TGA/DSC1, Switzerland), in the temperature from 30–850 °C.

Fourier Transform Infrared Spectroscopy (FTIR, Thermo Fisher Scientific Nicolet iS20, USA) characterization of AAMs powder samples at 4 cm⁻¹ wave number intervals in the wave number range of 400–4000 cm⁻¹.

Atomic force microscope (AFM, Bruker Dimension ICON, USA) is used to measure the elastic modulus of gel. Select an area of 10 μm x 10 μm for each AAMs sample, with a sampling rate set to 256 \times 256. All samples were polished before testing. Based on expert experience, the data of three gel areas are selected from each sample and collected to draw a boxplot. The size of a single gel area is 1 μm x 1 μm . Therefore, approximately 81 data points are included for each sample group. The sampling method is also applicable to the investigation of the interface transition zone of the AAMs samples.

X-ray computed tomography analysis (X-CT, ZEISS Xradia 515 Versa, Germany) was used to nondestructively observe the pore evolution and crack growth of different AAMs samples. The AAMs samples were crushed into particles of about 1 mm and scanned for 2 hours at an scan energy of 80 kV, 7 W. 3D modeling as well as pore identification was performed using post-processing software (Dragonfly, v 2024.1 Build 1613). Specifically, pore identification and segmentation based on image gray scale thresholding. Afterwards, porosity in 2D slices (763 layers in total, slice thickness = 1.5 μ m) along the z-axis direction was calculated layer by layer.

Carbon footprint analysis of AAMs

The life cycle assessment software SimaPro 9.5 was used for carbon footprint analysis under different scenarios with the standard ISO 14044 (2006). Most of the energy consumption data came from the Ecoinvent v3.9.1 database, such as the energy consumed by production units for electricity, heat, and alkali active agents. In order to compare the carbon emissions of ordinary cement, the boundary of this study starts with the production of raw materials and ends with the completion of alkali-activated material curing, excluding subsequent product transportation and sales (Supplementary Fig. 10). The 8 processes that generate GHG emissions are classified into four sectors: heat production, alkaline activator production, transportation, and electricity production. The list of parameters used for calculation was shown in Supplementary Table 3.

The IPCC 2021 GWP100 V1.02 method was used to calculate carbon emission intensity. The standard data of chemical substance and the energy consumption of each process are shown in Supplementary Tables 4–7. The uncertainty analysis was completed using the Monte Carlo simulation tool provided by the SimaPro 9.5 software, with a runtime set to n = 5000. The confidence interval is considered to be 95%. Accordingly, the GHG emission ranges under each aams preparation process were determined, and further box plots and probability distribution maps were drawn.

For microwave curing, the operating power and duration of the transmitter are known. After microwave curing, AAMs are kept in the microwave oven for 5 minutes. During this process, there are no other containers or materials that absorb microwaves, and it is assumed that the microwaves are completely absorbed by AAMs. Therefore, the microwave power density and energy efficiency is used to estimate the electricity consumption of microwave curing.

However, the power of the heater is constantly fluctuating during oven curing, making it difficult to calculate the energy consumption accurately. This is likely influenced by heat loss, heating regime, and hearth intensity. It is well known that the energy efficiency of thermal equipment increases rapidly with the intensity of the load and the size of the equipment. As a result, the thermal efficiency of heating furnaces for industrial applications is much higher than that of laboratory ovens. This means that many studies on the carbon footprint of oven curing may have overestimated its energy consumption. Therefore, an indirect method was proposed to investigative energy emissions from oven curing, as the thermal efficiency of industrial heating equipment was commonly known. It was feasible to monitor the energy required to cure 1 unit mass of AAMs at 70 °C for 6 hours, based on the following Eq. (2):

$$Q_{real} = \frac{Q_{AAMs}}{\eta} = \frac{(Q_{loaded} - Q_{empty})}{\eta}$$
 (2)

where, Q_{real} represents the energy consumption of oven curing for actual industrial use. Q_{AAMs} represent the energy consumed by oven curing for unit mass AAMs. Q_{loaded} represents the data monitored by a wattmeter when the oven is loaded with unit mass AAMs. Q_{empty} represents the data monitored by the electricity meter when the oven is empty. η represents the thermal efficiency of industrial heating equipment. Considering the low temperature of oven curing, the actual thermal efficiency was assumed to be $40\text{-}60\%^{40\text{-}41}$. Q_{loaded} and Q_{empty} are taken as the average of three measurements (n = 3). Similarly, the energy consumption of drying the WSS sample was measured using this method and recorded in Supplementary Table 4.

The calculation of the impact of using steel slag-based AAMs as substitutes on GHG emissions from cement manufacturing (2020–2050) is detailed in Supplementary Table 9 and Supplementary Note 4.

Data availability

The authors declare that the data supporting the findings of this study are available within the paper and its supplementary information files. Source data are provided with this paper.

References

- Seymour, L. M. et al. Hot mixing: Mechanistic insights into the durability of ancient Roman concrete. Sci. Adv. 9, eadd1602 (2023).
- 2. Cheng, D. et al. Projecting future carbon emissions from cement production in developing countries. *Nat. Commun.* **14**, 8213 (2023).
- IEA. Cement. (IEA, Paris, 2023); https://www.iea.org/reports/ cement-3.
- Wang, W., Noguchi, T. & Maruyama, I. Mechanism understanding of alkali-silica reaction in alkali-activated materials system. *Cem. Concr. Res.* 156, 106768 (2022).
- Gao, W. et al. Comprehensive utilization of steel slag: A review. Powder Technol. 422, 118449 (2023).

- 6. Liu, Y., Gu, F., Zhou, H., Li, Q. & Shang, S. Study on the performance and reaction mechanism of alkali-activated clay brick with steel slag and fly ash. *Constr. Build. Mater.* **411**, 134406 (2024).
- Song, W. et al. Effect of steel slag on fresh, hardened and microstructural properties of high-calcium fly ash based geopolymers at standard curing condition. Constr. Build. Mater. 229, 116933 (2019).
- Bai, T., Song, Z.-G., Wu, Y.-G., Hu, X.-D. & Bai, H. Influence of steel slag on the mechanical properties and curing time of metakaolin geopolymer. Ceram. Int. 44, 15706–15713 (2018).
- Liu, J. et al. Synthesis of geopolymer using municipal solid waste incineration fly ash and steel slag: Hydration properties and immobilization of heavy metals. J. Environ. Manag. 341, 118053 (2023).
- Martins, A. C. P. et al. Steel slags in cement-based composites: An ultimate review on characterization, applications and performance. Constr. Build. Mater. 291, 123265 (2021).
- Fisher, L. V. & Barron, A. R. The recycling and reuse of steelmaking slags — A review. Resour. Conserv. Recycling 146, 244–255 (2019).
- Jiang, Y., Ling, T.-C., Shi, C. & Pan, S.-Y. Characteristics of steel slags and their use in cement and concrete—A review. Resour. Conserv. Recycl. 136, 187–197 (2018).
- Wang, Y.-f, Huang, X., Zhang, S.-G., Ma, W. & Li, J.-S. Utilization of ultra-fine solid waste in the sustainable cementitious material for enhanced performance. Constr. Build. Mater. 417, 135239 (2024).
- Hu, J. Comparison between the effects of superfine steel slag and superfine phosphorus slag on the long-term performances and durability of concrete. J. Therm. Anal. Calorim. 128, 1251–1263 (2017).
- Yang, Z. et al. Effect of fineness on the hydration and microstructure of cementitious materials with high-volume steel slag and blast furnace slag. J. Build. Eng. 72, 106682 (2023).
- Wang, Q., Yang, J. & Yan, P. Cementitious properties of super-fine steel slag. Powder Technol. 245, 35–39 (2013).
- Yang, Z., Dong, S. & Zhang, Y. Particle packing optimization and pore structure assessment of ternary cementitious system based on X-ray computed tomography and mercury intrusion porosimetry. Constr. Build. Mater. 413, 134913 (2024).
- Duan, S., Liao, H., Song, H., Cheng, F. & Yang, H. Performance improvement to ash-cement blocks by adding ultra-fine steel slag collected from a supersonic steam-jet smasher. *Constr. Build. Mater.* 212, 140–148 (2019).
- Ravikumar, D. et al. Carbon dioxide utilization in concrete curing or mixing might not produce a net climate benefit. *Nat. Commun.* 12, 855 (2021).
- Zajac, M., Maruyama, I., Iizuka, A. & Skibsted, J. Enforced carbonation of cementitious materials. Cem. Concr. Res. 174, 107285 (2023).
- 21. Zhou, Z. et al. Long-term volume stability of steel slag sand mortar and concrete. *Case Stud. Constr. Mater.* **22**, e04179 (2025).
- 22. Zhao, J. et al. Effect of environment conditions on volume deformation of blended cement mortars containing blast furnace slag and steel slag powder. *J. Build. Eng.* **85**, 108692 (2024).
- Villca, A. R. et al. Lime/pozzolan/geopolymer systems: Performance in pastes and mortars. Constr. Build. Mater. 276, 122208 (2021).
- 24. Scrivener, K., Ouzia, A., Juilland, P. & Kunhi Mohamed, A. Advances in understanding cement hydration mechanisms. *Cem. Concr. Res.* **124**, 105823 (2019).
- Kang, S.-H., Jeong, Y., Kim, M. O. & Moon, J. Pozzolanic reaction on alkali-activated Class F fly ash for ambient condition curable structural materials. Constr. Build. Mater. 218, 235–244 (2019).
- Nath, S. K. & Kumar, S. Role of particle fineness on engineering properties and microstructure of fly ash derived geopolymer. Constr. Build. Mater. 233, 117294 (2020).
- Amran, M., Debbarma, S. & Ozbakkaloglu, T. Fly ash-based ecofriendly geopolymer concrete: A critical review of the long-term durability properties. Constr. Build. Mater. 270, 121857 (2021).

- Sun, Y. et al. A review on microwave irradiation to the properties of geopolymers: Mechanisms and challenges. Constr. Build. Mater. 294, 123491 (2021).
- Qing, L., Shaokang, S., Zhen, J., Junxiang, W. & Xianjun, L. Effect of CaO on hydration properties of one-part alkali-activated material prepared from tailings through alkaline hydrothermal activation. Constr. Build. Mater. 308, 124931 (2021).
- Al-Ostaz, A., Wu, W., Cheng, A. H. D. & Song, C. R. A molecular dynamics and microporomechanics study on the mechanical properties of major constituents of hydrated cement. *Compos. Part* B: Eng. 41, 543–549 (2010).
- Fu, J., Kamali-Bernard, S., Bernard, F. & Cornen, M. Comparison of mechanical properties of C-S-H and portlandite between nanoindentation experiments and a modeling approach using various simulation techniques. *Compos. Part B: Eng.* 151, 127–138 (2018).
- 32. Cancio Díaz, Y. et al. Limestone calcined clay cement as a low-carbon solution to meet expanding cement demand in emerging economies. *Dev. Eng.* **2**, 82–91 (2017).
- Sánchez Berriel, S. et al. Assessing the environmental and economic potential of Limestone Calcined Clay Cement in Cuba. J. Clean. Prod. 124, 361–369 (2016).
- Arruda Junior, E. S., de Sales Braga, N. T. & Barata, M. S. Life cycle assessment to produce LC³ cements with kaolinitic waste from the Amazon region, Brazil. Case Stud. Constr. Mater. 18, e01729 (2023).
- IEA. Technology Roadmap Low-Carbon Transition in the Cement Industry. https://www.iea.org/reports/technologyroadmap-low-carbon-transition-in-the-cement-industry (IEA, Paris, 2018).
- Gultekin, A. & Ramyar, K. Investigation of high-temperature resistance of natural pozzolan-based geopolymers produced with oven and microwave curing. Constr. Build. Mater. 365, 130059 (2023).
- Alqahtani, F. K., Rashid, K., Zafar, I. & Iqbal Khan, M. Assessment of morphological characteristics and physico-mechanical properties of geopolymer green foam lightweight aggregate formulated by microwave irradiation. J. Build. Eng. 35, 102081 (2021).
- 38. Shah, I. H., Miller, S. A., Jiang, D. & Myers, R. J. Cement substitution with secondary materials can reduce annual global CO2 emissions by up to 1.3 gigatons. *Nat. Commun.* **13**, 5758 (2022).
- Kong, Y., Wang, P., Liu, S. & Gao, Z. Hydration and microstructure of cement-based materials under microwave curing. *Constr. Build. Mater.* 114, 831–838 (2016).
- 40. Han, S. H., Chang, D. & Huh, C. Efficiency analysis of radiative slab heating in a walking-beam-type reheating furnace. *Energy* **36**, 1265–1272 (2011).
- 41. Zhao, J. et al. Industrial reheating furnaces: A review of energy efficiency assessments, waste heat recovery potentials, heating process characteristics and perspectives for steel industry. *Process Saf. Environ. Prot.* **147**, 1209–1228 (2021).
- Crude steel production by process 2022. https://worldsteel.org/ data/world-steel-in-figures-2023/ (Worldsteel Association, Belgium, 2023).
- Snellings, R., Suraneni, P. & Skibsted, J. Future and emerging supplementary cementitious materials. *Cem. Concr. Res.* 171, 107199 (2023).
- 44. Juenger, M. C. G., Snellings, R. & Bernal, S. A. Supplementary cementitious materials: New sources, characterization, and performance insights. *Cem. Concr. Res.* **122**, 257–273 (2019).
- Wang, S., Lin, X., Zhang, Y. & Wang, C. A review of utilizing carbide slag to sequestrate carbon dioxide by mineral carbonation: Mechanisms, processes, and value-added products. *Fuel* 384, 134041 (2025).
- Xie, G. et al. High-value utilization of modified magnesium slag solid waste and its application as a low-carbon cement admixture. *J. Environ. Manag.* 349, 119551 (2024).

Acknowledgements

This work was supported by the Natural Science Foundation of Shandong Province (Project no. ZR202105290004) from the Science and Technology Department of Shandong Province, China. Specifically, the author thanks Carl Zeiss (Shanghai) Co. Ltd., and Xianghu Technology Development Co., Ltd. (Beijing, China) for their technical support in optics, microwave, etc. Finally, the author thanks Dr. Xueqiang Zhang, Dr. Wenbo Zhang, and Dr. Xiangguo Zhang from Beijing University of Science and Technology for their assistance in explaining the solidification behavior of the SS/WSS slurry.

Author contributions

B.Y.H. designed the study and wrote the paper. X.Y.Z. and Y.X.L. participated in carbon footprint analysis and figure drawing. X.H.J., Y.L., and Z.H.C. participated in text inspection and gelling mechanism discussion. D.Q.C., J.P.B., and Z.A.T. participated in the discussion of the introduction and supervision. L.L.Z. participated in validation, supervision, writing, and discussion. All authors reviewed the manuscript.

Competing interests

The authors declare no competing interests.

Additional information

Supplementary information The online version contains supplementary material available at https://doi.org/10.1038/s41467-025-62488-1.

Correspondence and requests for materials should be addressed to Lingling Zhang.

Peer review information *Nature Communications* thanks the anonymous reviewers for their contribution to the peer review of this work. A peer review file is available.

Reprints and permissions information is available at http://www.nature.com/reprints

Publisher's note Springer Nature remains neutral with regard to jurisdictional claims in published maps and institutional affiliations.

Open Access This article is licensed under a Creative Commons Attribution-NonCommercial-NoDerivatives 4.0 International License, which permits any non-commercial use, sharing, distribution and reproduction in any medium or format, as long as you give appropriate credit to the original author(s) and the source, provide a link to the Creative Commons licence, and indicate if you modified the licensed material. You do not have permission under this licence to share adapted material derived from this article or parts of it. The images or other third party material in this article are included in the article's Creative Commons licence, unless indicated otherwise in a credit line to the material. If material is not included in the article's Creative Commons licence and your intended use is not permitted by statutory regulation or exceeds the permitted use, you will need to obtain permission directly from the copyright holder. To view a copy of this licence, visit http://creativecommons.org/licenses/by-nc-nd/4.0/.

© The Author(s) 2025